The Astrophysical Journal, 850:1 (8pp), 2017 November 20 https://doi.org/10.3847/1538-4357/aa8ccf

Rise of the Titans: A Dusty, Hyper-luminous "870 μm Riser" Galaxy at $z \sim 6$

Dominik A. Riechers[1], T. K. Daisy Leung[1], Rob J. Ivison[2,3], Ismael Pérez-Fournon[4,5], Alexander J. R. Lewis[3], Rui Marques-Chaves[4,5], Iván Oteo[2,3], Dave L. Clements[6], Asantha Cooray[7], Josh Greenslade[6], Paloma Martínez-Navajas[4,5], Seb Oliver[8], Dimitra Rigopoulou[9,10], Douglas Scott[11], and Axel Weiss[12]
[1] Cornell University, Space Sciences Building, Ithaca, NY 14853, USA; riechers@cornell.edu
[2] European Southern Observatory, Karl-Schwarzschild-Straße 2, D-85748 Garching, Germany
[3] Institute for Astronomy, University of Edinburgh, Royal Observatory, Blackford Hill, Edinburgh EH9 3HJ, UK
[4] Instituto de Astrofisica de Canarias, E-38200 La Laguna, Tenerife, Spain
[5] Departamento de Astrofisica, Universidad de La Laguna, E-38205 La Laguna, Tenerife, Spain
[6] Astrophysics Group, Imperial College London, Blackett Laboratory, Prince Consort Road, London SW7 2AZ, UK
[7] Department of Physics and Astronomy, University of California, Irvine, CA 92697, USA
[8] Astronomy Centre, Department of Physics and Astronomy, University of Sussex, Brighton BN1 9QH, UK
[9] Department of Physics, University of Oxford, Keble Road, Oxford OX1 3RH, UK
[10] Space Science and Technology Department, Rutherford Appleton Laboratory, Chilton, Didcot, Oxfordshire OX11 0QX, UK
[11] Department of Physics and Astronomy, University of British Columbia, 6224 Agricultural Road, Vancouver, BC V6T 1Z1, Canada
[12] Max-Planck-Institut für Radioastronomie, Auf dem Hügel 69, D-53121 Bonn, Germany
Received 2017 May 25; revised 2017 August 31; accepted 2017 September 12; published 2017 November 13

Abstract

We report the detection of ADFS-27, a dusty, starbursting major merger at a redshift of $z = 5.655$, using the Atacama Large Millimeter/submillimeter Array (ALMA). ADFS-27 was selected from *Herschel*/Spectral and Photometric Imaging Receiver (SPIRE) and APEX/LABOCA data as an extremely red "870 μm riser" (i.e., $S_{250\,\mu\mathrm{m}} < S_{350\,\mu\mathrm{m}} < S_{500\,\mu\mathrm{m}} < S_{870\,\mu\mathrm{m}}$), demonstrating the utility of this technique to identify some of the highest-redshift dusty galaxies. A scan of the 3 mm atmospheric window with ALMA yields detections of CO($J = 5 \rightarrow 4$) and CO($J = 6 \rightarrow 5$) emission, and a tentative detection of $H_2O(2_{11} \rightarrow 2_{02})$ emission, which provides an unambiguous redshift measurement. The strength of the CO lines implies a large molecular gas reservoir with a mass of $M_{\mathrm{gas}} = 2.5 \times 10^{11}\,(\alpha_{\mathrm{CO}}/0.8)(0.39/r_{51})\,M_{\odot}$, sufficient to maintain its $\sim$2400 $M_{\odot}$ yr^{-1} starburst for at least $\sim$100 Myr. The 870 μm dust continuum emission is resolved into two components, 1.8 and 2.1 kpc in diameter, separated by 9.0 kpc, with comparable dust luminosities, suggesting an ongoing major merger. The infrared luminosity of $L_{\mathrm{IR}} \simeq 2.4 \times 10^{13}\,L_{\odot}$ implies that this system represents a binary hyper-luminous infrared galaxy, the most distant of its kind presently known. This also implies star formation rate surface densities of $\Sigma_{\mathrm{SFR}} = 730$ and 750 $M_{\odot}$ yr^{-1} kpc^2, consistent with a binary "maximum starburst." The discovery of this rare system is consistent with a significantly higher space density than previously thought for the most luminous dusty starbursts within the first billion years of cosmic time, easing tensions regarding the space densities of $z \sim 6$ quasars and massive quiescent galaxies at $z \gtrsim 3$.

Key words: cosmology: observations – galaxies: active – galaxies: formation – galaxies: high-redshift – galaxies: starburst – radio lines: galaxies

1. Introduction

Detailed studies of dusty star-forming galaxies (DSFGs) at high redshift selected at (sub)millimeter wavelengths (submillimeter galaxies, or SMGs) over the past two decades have shown them to be a key ingredient in our understanding of the early formation of massive galaxies (see Blain et al. 2002; Casey et al. 2014 for reviews). The brightest, "hyper-luminous" DSFGs (hyper-luminous infrared galaxies, or HyLIRGs) represent some of the most luminous, massive galaxies in the early universe, reaching infrared luminosities of $L_{\mathrm{IR}} > 10^{13}\,L_{\odot}$, and star formation rates (SFRs) in excess of 1000 $M_{\odot}$ yr^{-1}, emerging from compact regions only a few kiloparsecs in diameter (e.g., Riechers et al. 2013; Fu et al. 2013; Ivison et al. 2013; Riechers et al. 2014; Hodge et al. 2015, 2016; Oteo et al. 2016). While the general DSFG population is thought to be somewhat heterogeneous (e.g., Davé et al. 2010; Narayanan et al. 2010, 2015; Hayward et al. 2012), these HyLIRGs are likely major mergers of gas-rich galaxies (e.g., Engel et al. 2010; Riechers et al. 2011; Ivison et al. 2011, 2013; Oteo et al. 2016), and they may also be associated with protoclusters of galaxies, which represent some of the most overdense environments in the early universe (e.g., Daddi et al. 2009; Capak et al. 2011; Ivison et al. 2013).

Due to their high dust content, it is common that most of the stellar light in DSFGs is subject to dust extinction, rendering their identification out to the highest redshifts notoriously difficult. While many DSFGs were found at $z = 2$–3.5 relatively early on (e.g., Ivison et al. 1998, 2000; Chapman et al. 2005), more than a decade passed between the initial discovery of this galaxy population and the identification of the first examples at $z > 4$ (Capak et al. 2008; Daddi et al. 2009) and $z > 5$ (Riechers et al. 2010; Capak et al. 2011; Walter et al. 2012).

Once the *Herschel Space Observatory* was launched, it became possible to develop color selection techniques to systematically search for the most distant DSFGs in large-area surveys like the *Herschel* Multi-tiered Extragalactic Survey (HerMES; Oliver et al. 2012). Since the peak of the far-infrared (FIR) spectral energy distribution (SED) shifts through the 250, 350, and 500 μm bands probed by *Herschel*'s Spectral and Photometric Imaging Receiver (SPIRE), the most distant sources typically appear "red" between these bands, i.e., $S_{250\,\mu\mathrm{m}} < S_{350\,\mu\mathrm{m}} < S_{500\,\mu\mathrm{m}}$, with steeper ("ultra-red") color

criteria resulting in the selection of potentially more distant sources (e.g., Riechers et al. 2013; Ivison et al. 2016). Based on FIR photometric redshift estimates, the median redshifts of these sources have been suggested to be $\langle z \rangle = 3.7$ to 4.7, where different redshift values are obtained for different samples due to the exact color cutoffs, flux density limits, and redshift fitting techniques chosen (e.g., Dowell et al. 2014; Ivison et al. 2016; see also Asboth et al. 2016). Spectroscopic confirmation of a subsample of 25 sources based on CO rotational lines, an indicator of the molecular gas that fuels the intense star formation in these systems (see Carilli & Walter 2013 for a review), has verified the higher median redshifts compared to general DSFG samples (e.g., Cox et al. 2011; Combes et al. 2012; Riechers et al. 2013; D. Riechers et al. 2017, in preparation; Fudamoto et al. 2017). These studies find redshifts as high as $z = 6.34$ (Riechers et al. 2013). In an alternative approach, surveys with the South Pole Telescope (SPT) have revealed a sample of gravitationally lensed DSFGs selected at 1.4 and 2 mm with a spectroscopic median redshift of $\langle z \rangle = 3.9$ (e.g., Weiss et al. 2013; Strandet et al. 2016). A substantial fraction of this sample would also fulfill *Herschel*-red sample selection criteria.

With this paper, we aim to extend the *Herschel*-red and ultra-red criteria through the identification of "extremely red" DSFGs with $S_{250\,\mu m} < S_{350\,\mu m} < S_{500\,\mu m} < S_{870\,\mu m}$. Such "870 μm riser" galaxies should, in principle, lie at even higher redshifts than the bulk of the red DSFG population. We here present detailed follow-up observations of the first such source we have identified in the *Herschel* HerMES data, 2HERMES S250 SF J043657.7–543810 (hereafter: ADFS-27). We use a concordance, flat ΛCDM cosmology throughout, with $H_0 = 69.6$ km s^{-1} Mpc^{-1}, $\Omega_M = 0.286$, and $\Omega_\Lambda = 0.714$.

2. Data

2.1. Herschel/PACS+SPIRE

ADFS-27 was observed with the *Herschel Space Observatory* as part of HerMES, covering 7.47 deg^2 in the Akari Deep Field South (ADFS). The field was observed for 18.1 hr with the PACS and SPIRE instruments in parallel mode, resulting in nominal instrumental noise levels of 49.9, 95.1, 25.8, 21.2, and 30.8 mJy (5σ rms) at 110, 160, 250, 350, and 500 μm, respectively.[13] The flux scale is accurate to ∼5%. ADFS-27 was detected at 250, 350, and 500 μm, but not shortwards. Flux densities were extracted using *Starfinder* and *SussExtractor*, and from the band-merged xID250 catalog published as part of HerMES DR4. This yields $S_{250\,\mu m} = (14.3 \pm 2.3)$, (13.0 ± 2.6), and (14.3 ± 2.3) mJy, $S_{350\,\mu m} = (20.3 \pm 2.4)$, (18.5 ± 2.5), and (19.1 ± 2.3) mJy, and $S_{500\,\mu m} = (22.0 \pm 2.6)$, (22.2 ± 2.9), and (24.0 ± 2.7) mJy, respectively. These uncertainties do not include a contribution due to source confusion, which typically dominates. However, we note that the source is relatively isolated in the SPIRE maps (Figure 1). xID250-based flux densities are adopted in the following (Table 1). From these data, ADFS-27 was selected as a "red source" (i.e., $S_{250\,\mu m} < S_{350\,\mu m} < S_{500\,\mu m}$) for further follow-up observations.

[13] Quoted sensitivities are single-pixel rms values, which are worse than the flux uncertainties of point sources achieved after employing matched filtering techniques (e.g., Oliver et al. 2012; Schulz et al. 2017).

2.2. APEX/LABOCA

We observed ADFS-27 at 870 μm with the Large APEX bolometer camera (LABOCA) mounted on the 12 m Atacama Pathfinder EXperiment (APEX) telescope. Observations were carried out on 2012 September 17 as part of program M-090.F-0025-2012, resulting in 3.4 hr on-source time. Individual scans had a length of ∼7 minutes, resulting in a map that fully samples the ∼11 arcmin diameter field of view of LABOCA. Pointing was checked on nearby quasars every hour, and was stable to within ∼3″ rms. The effective FWHM beam size, as measured on the pointing source J2258–280, was 19.″2. Precipitable water vapor columns varied between 0.4 and 1.3 mm, corresponding to zenith atmospheric opacities of 0.2–0.4 in the LABOCA passband. This resulted in an rms noise level of 1.8 mJy beam^{-1} at the position of ADFS-27 (3.7 mJy beam^{-1} map average) in a map smoothed to 27″ resolution. The flux density scale was determined through observations of Uranus and Neptune, yielding an accuracy of ∼7%. Data reduction was performed with the *BoA* package, applying standard calibration techniques. These observations were used to select ADFS-27 as an "extremely red" source with $S_{250\,\mu m} < S_{350\,\mu m} < S_{500\,\mu m} < S_{870\,\mu m}$ (Figure 1; Table 1).

2.3. ALMA 870 μm

We observed 870 μm continuum emission toward ADFS-27 using the Atacama Large Millimeter/submillimeter Array (ALMA; project ID: 2013.1.00001.S; PI: Ivison). Observations were carried out on 2015 August 31 with 33 usable 12 m antennas under good weather conditions in an extended array configuration (baseline range: 15–1466 m). This resulted in 5.1 minutes of usable on-source time, centered on the *Herschel*/SPIRE 500 μm position. The nearby quasar J0425–5331 was observed regularly for pointing, amplitude, and phase calibration, while J0538–4405 was observed for bandpass calibration, and J0519–4546 was used for absolute flux calibration, leading to <10% calibration uncertainty. The correlator was set up with two spectral windows of 1.875 GHz bandwidth (dual polarization) each per sideband, centered at a local oscillator frequency of 343.463325 GHz, with a frequency gap of 8 GHz between the sidebands.

Data reduction was performed using version 4.7.1 of the Common Astronomy Software Applications (CASA) package. Data were mapped using the CLEAN algorithm with "natural" and robust 0.5 weighting, resulting in synthesized beam sizes of 0.″20 × 0.″17 and 0.″17 × 0.″14 at rms noise values of 99 and 108 μJy beam^{-1} in the phase center over the entire 7.5 GHz bandwidth, respectively. Due to its distance from the phase center, the noise is increased by a primary beam attenuation factor of 1.62 at the position of ADFS-27.

2.4. ALMA 3 mm

We scanned the 84.077033–113.280277 GHz frequency range to search for spectral lines toward ADFS-27 using ALMA (project ID: 2016.1.00613.S; PI: Riechers). Observations were carried out under good weather conditions during six runs between 2017 January 5 and 9 with 40–47 usable 12 m antennas in a compact array configuration (baseline range: 15–460 m). We used five spectral setups, resulting in a total on-source time of 45.7 minutes (7.8–14.1 minutes per setup), centered on the ALMA 870 μm position. The nearby quasar J0425–5331 was observed regularly for pointing, amplitude, and phase calibration. J0519–4546 was used for

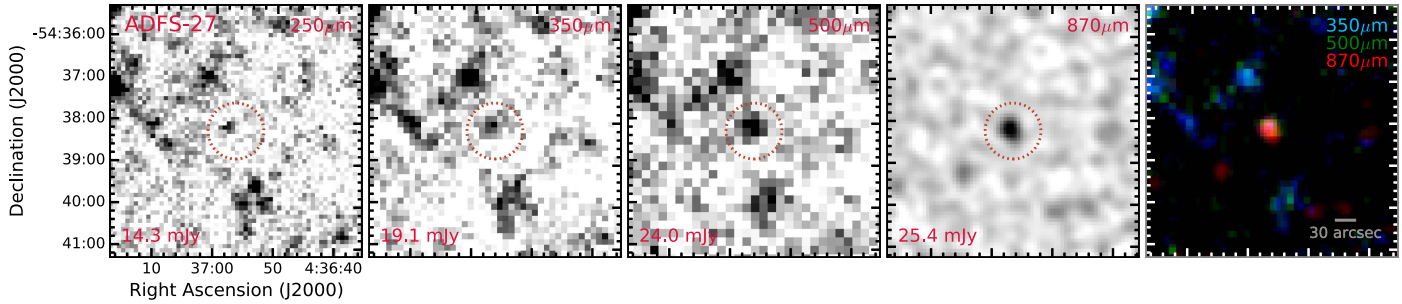

Figure 1. *Herschel*/SPIRE 250, 350, and 500 μm and APEX/LABOCA 870 μm images centered on ADFS-27, and 870/500/350 μm color composite (left to right). Source flux densities are indicated in the bottom left corners of the first four panels (see Table 1 for uncertainties). The source is relatively isolated in the deep SPIRE maps.

Table 1
ADFS-27 Continuum Photometry

Wavelength (μm)	Flux Density[a] (mJy)	Telescope
1.25	<0.015	VISTA/VHS
1.65	<0.022	VISTA/VHS
2.15	<0.020	VISTA/VHS
3.6[b]	$(2.33 \pm 0.74) \times 10^{-3}$	*Spitzer*/IRAC
4.5[b]	$(4.20 \pm 0.82) \times 10^{-3}$	*Spitzer*/IRAC
12	<0.6	*WISE*
22	<3.6	*WISE*
110	<30	*Herschel*/PACS
160	<57	*Herschel*/PACS
250[c,d]	14.3 ± 2.3	*Herschel*/SPIRE
350[c,d]	19.1 ± 2.3	*Herschel*/SPIRE
500[c,d]	24.0 ± 2.7	*Herschel*/SPIRE
870[c]	25.4 ± 1.8	APEX/LABOCA
870	28.1 ± 0.9	ALMA
3000	0.512 ± 0.023	ALMA (scan)

Notes.
[a] Limits are 3σ.
[b] Possibly contaminated by foreground sources, and hence, considered as upper limits only in the SED fitting.
[c] Used for initial color/photometric redshift selection.
[d] Uncertainties do not account for confusion noise, which is 5.9, 6.3, and 6.8 mJy (1σ) at 250, 350, and 500 μm, respectively (Nguyen et al. 2010).

bandpass and absolute flux calibration, leading to <10% calibration uncertainty.

The correlator was set up with two spectral windows of 1.875 GHz bandwidth (dual polarization) each per sideband, at a sideband separation of 8 GHz. Full frequency coverage was attained by shifting setups in frequency by ~3.75 GHz, such that subsequent settings filled in part of the IF gap in the first spectral setup. This allowed us to cover the full range of ~29.21 GHz without significant gaps in frequency, but resulted in some frequency overlap near 97.5 GHz (see Figure 2 for effective exposure times across the full band).

Data reduction was performed using version 4.7.1 of the CASA package. Data were mapped using the CLEAN algorithm with "natural" and robust 0.5 weighting, resulting in synthesized beam sizes of $3\farcs13 \times 2\farcs36$ and $2\farcs48 \times 1\farcs86$ at rms noise values of 11.2 and 13.6 μJy beam^{-1} in the phase center over a line-free bandwidth of 27.40 GHz after averaging all spectral setups, respectively. Spectral line cubes mapped with "natural" weighting at 86.6, 103.9, and 113.0 GHz yield beam sizes of $3\farcs68 \times 2\farcs72$, $3\farcs05 \times 2\farcs26$, and $2\farcs83 \times 2\farcs17$ at rms noise levels of 352, 509, and 297 μJy beam^{-1} per 19.55, 19.55, and 58.65 MHz bin, respectively. Imaging the same data at 103.9 GHz with robust –2 ("uniform") weighting yields a beam size of $2\farcs11 \times 1\farcs56$ at ~1.9 times higher rms noise.

2.5. Spitzer/IRAC

ADFS-27 was covered with *Spitzer*/IRAC at 3.6 and 4.5 μm between 2011 November 17–21 (program ID: 80039; PI: Scarlata) and targeted for deeper observations on 2015 May 24 (program ID: 11107; PI: Perez-Fournon). Data reduction was performed using the *MOPEX* package using standard procedures. Absolute astrometry was obtained relative to *Gaia* DR1, yielding rms accuracies of $0\farcs04$ and $0\farcs06$ in the 3.6 and 4.5 μm bands, respectively. Photometry was obtained with the *SExtractor* package, after deblending from two foreground objects and sky removal using *GALFIT*.

2.6. VISTA and WISE

The position of ADFS-27 was covered by the VISTA Hemisphere Survey (VHS) DR4 on 2010 November 19 and by the *Wide-field Infrared Survey Explorer* (*WISE*) as part of the allWISE survey between 2010 January 19 and 2011 January 30. ADFS-27 is not detected in the VHS 1.25, 1.65, and 2.15 μm ($J/H/K_s$) bands. It is strongly blended with a nearby star ($m_{\rm gaia} = 18.20$) in the 3.4 and 4.6 μm (W1 and W2) bands, such that no useful limit can be obtained. It also remains undetected in the 12 and 22 μm (W3 and W4) bands.

3. Results

3.1. Continuum Emission

We detect strong continuum emission at 3 mm and 870 μm at peak significances of ~39 and 28σ toward ADFS-27, yielding flux densities of (0.512 ± 0.023) and (28.1 ± 0.9) mJy, respectively (Figures 2, bottom right and 3, respectively). The emission is marginally resolved at 3 mm, and it breaks up into two components of similar strength separated by $1\farcs49$ in the high-resolution 870 μm data, with flux densities of (15.70 ± 0.76) and (12.43 ± 0.56) mJy for the northern and southern components (hereafter, ADFS-27N, or "mal"말, the horse, and ADFS-27S, or "yong"용, the dragon), respectively.[14] The two components thus contain the full single-dish 870 μm flux. Both components are spatially resolved. Two-dimensional Gaussian fitting yields deconvolved sizes of (0.303 ± 0.030) × (0.213 ± 0.027) and (0.341 ± 0.031) × (0.146 ± 0.025) arcsec^2 for ADFS-27N

[14] Extracted from a map tapered to $0\farcs8$ resolution.

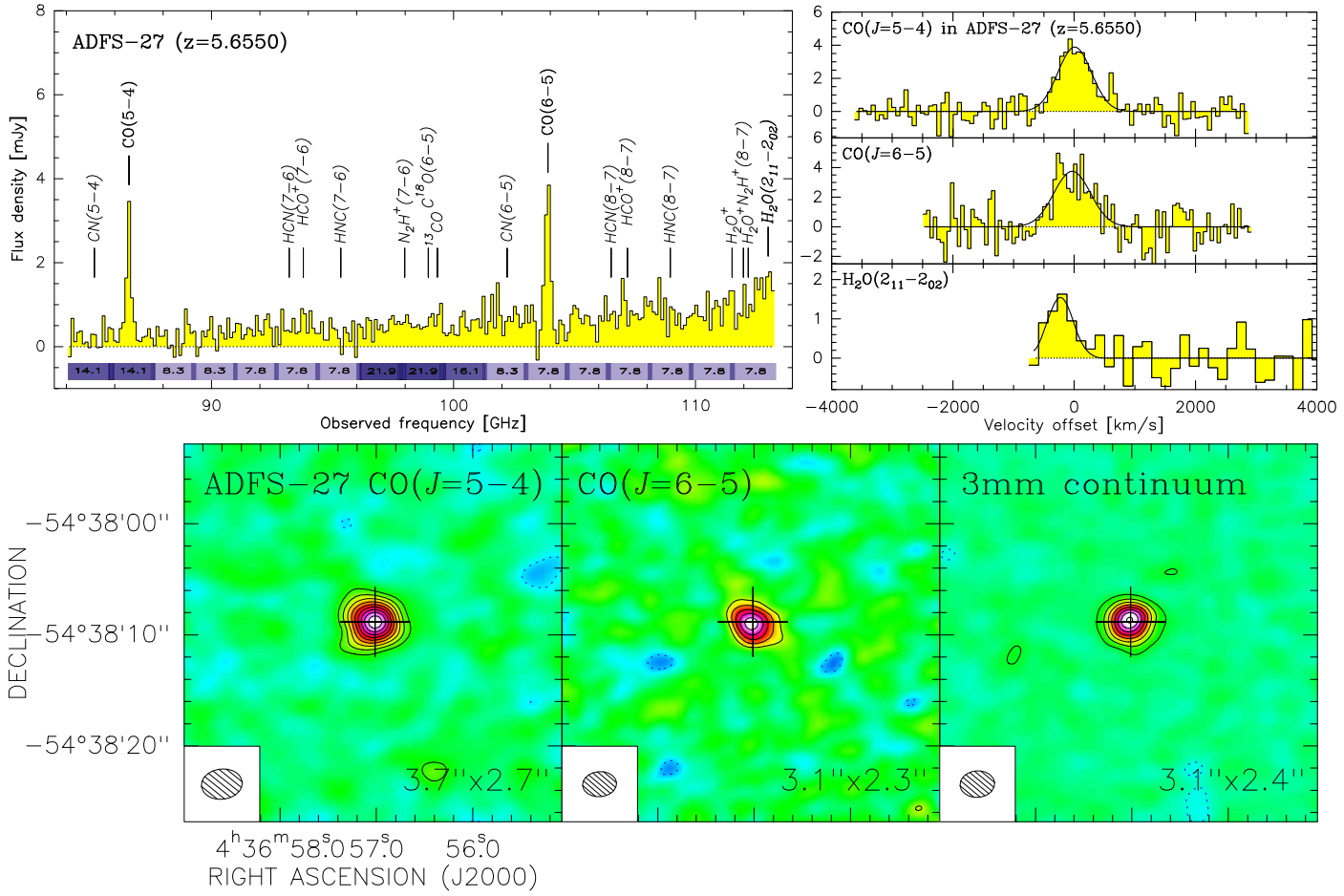

Figure 2. ALMA 3 mm spectra (top) and maps (bottom) of the line and continuum emission toward ADFS-27. Top left: full spectrum obtained after combination of all spectral setups at a spectral resolution of 117.3 MHz. The stripe near the bottom shows the integration time in minutes in each 1.875 GHz spectral window. Increasingly darker colors indicate regions covered by two or three observing runs due to repetition or tuning overlap. Top Right: zoom-in regions showing the spectral lines used for the redshift identification after continuum subtraction. The $H_2O(2_{11} \rightarrow 2_{02})$ line is only marginally detected. Spectra of the CO($J = 5 \rightarrow 4$), CO($J = 6 \rightarrow 5$), and $H_2O(2_{11} \rightarrow 2_{02})$ lines are shown at spectral resolutions of 19.55, 19.55, and 58.65 MHz (68, 56, and 156 km s^{-1}), respectively. Bottom: integrated line maps of the CO($J = 5 \rightarrow 4$) and CO($J = 6 \rightarrow 5$) emission over 651 and 711 km s^{-1}, and continuum map across the line-free spectral range (27.40 GHz), imaged with natural baseline weighting. The beam sizes are indicated in the bottom left corner of each panel. Contours are shown in steps of 2σ (lines) and 5σ (continuum), starting at 3σ, where $1\sigma = 0.084$ Jy km s^{-1} beam^{-1}, 0.12 Jy km s^{-1} beam^{-1}, and 11.2 μJy beam^{-1}, respectively. The cross in each panel indicates the peak position of the CO($J = 5 \rightarrow 4$) emission.

and S, respectively. After removal of a bright foreground star, some faint residual emission is seen at 3.6 and 4.5 μm near the position of ADFS-27 and consistent with the expected flux levels (Figure 4), but higher resolution observations would be required to confirm its mid-infrared detection (Figure 3; Table 1). Given the lack of a candidate lensing galaxy at short wavelengths or arc-like structure in the high-resolution ALMA data, there presently is no evidence for strong gravitational lensing (i.e., flux magnification factors $\mu_L \geqslant 2$), but detailed imaging with the *Hubble Space Telescope* would be required to further investigate the possibility of strong or weak lensing.

3.2. Line Emission

A search of the 3 mm spectral sweep reveals two strong features near 86.6 and 103.9 GHz detected at ∼19 and 12σ significance, respectively. Together with a third, tentative feature near 113.0 GHz recovered at 2.3σ significance, we obtain a unique (median) redshift solution at $z = 5.6550 \pm 0.0001$, identifying the features as CO($J = 5 \rightarrow 4$), CO($J = 6 \rightarrow 5$), and $H_2O(2_{11} \rightarrow 2_{02})$ emission (Figure 2, top).[15] The $H_2O(2_{11} \rightarrow 2_{02})$ line recovery is marginal at best and near the edge of the spectral range. Thus, an independent confirmation of this feature is required. The line emission is marginally resolved on the longest baselines and elongated along the axis that separates the two continuum source components, and thus, is consistent with emerging from both sources (Figure 5). From Gaussian fitting to the line profiles, we obtain peak flux densities of $S_{\rm line} = (3.89 \pm 0.28)$, (3.75 ± 0.43), and (1.55 ± 0.37) mJy at FWHM linewidths of dv = (651 ± 59), (710 ± 103), and (503 ± 163) km s^{-1}, respectively.[16] This implies integrated line fluxes of (2.68 ± 0.20), (2.82 ± 0.34), and (0.83 ± 0.22) Jy km s^{-1} and line luminosities of $L'_{\rm CO} = (11.96 \pm 0.92)$ and (8.73 ± 1.07) and $L'_{\rm H_2O} = (2.17 \pm 0.58) \times 10^{10}$ K km s^{-1} pc^2, respectively (Table 2). This yields a

[15] No spectral lines are detected in the ALMA 870 μm data.

[16] The CO line redshifts agree within $<1\sigma$, where $1\sigma = 25$ and 43 km s^{-1} for the CO $J = 5 \rightarrow 4$ and $6 \rightarrow 5$ lines, respectively. The fit of the $H_2O(2_{11} \rightarrow 2_{02})$ line indicates a blueshift by $-(237 \pm 64)$ km s^{-1} with respect to the CO($J = 5 \rightarrow 4$) line, which we consider to be due to a limited signal-to-noise ratio. Another possible explanation is that the H_2O emission may preferentially emerge from one of the components of ADFS-27, assuming a small centroid velocity shift between both components. Fixing the line centroid to that of the CO($J = 5 \rightarrow 4$) line yields $S_{\rm line} = (0.99 \pm 0.31)$ mJy and dv = (915 ± 380) km s^{-1}, i.e., a ∼15% higher line flux. This difference is not significant.

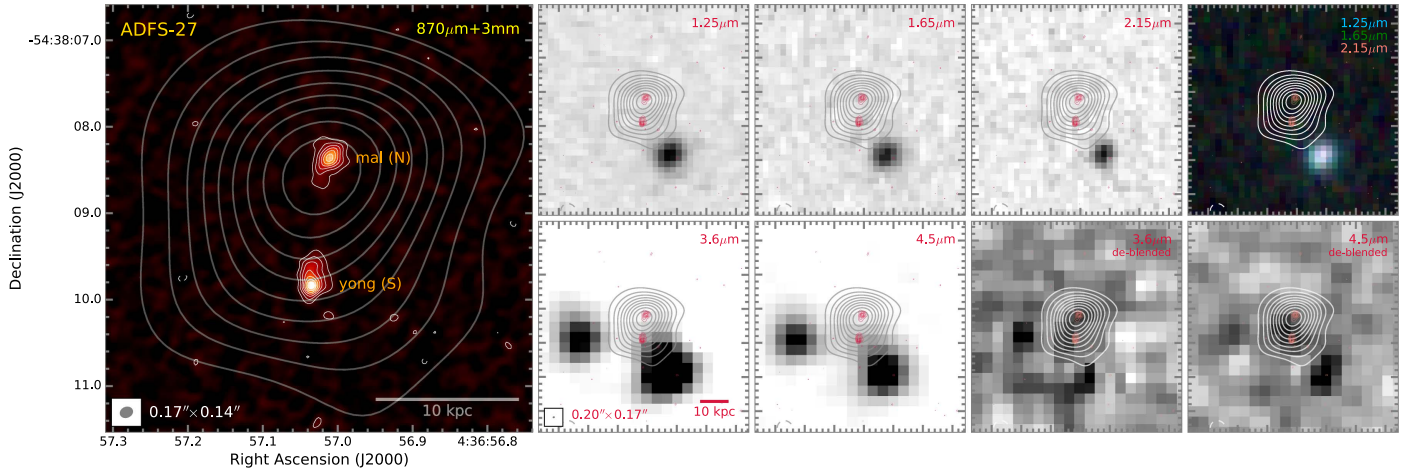

Figure 3. ALMA 870 μm, *Spitzer*/IRAC 3.6 and 4.5 μm, and VISTA 1.25, 1.65, and 2.15 μm imaging of ADFS-27. Left: 870 μm imaging (color scale and white contours) overlaid with 3 mm continuum contours (gray). Both data sets are imaged with robust 0.5 weighting. Bottom middle: 3.6 and 4.5 μm imaging overlaid with 870 μm (crimson color, natural weighting) and 3 mm continuum contours (same as left panel). Bottom right: same as middle, but with foreground sources subtracted and contrast adjusted. Top middle/right: VISTA images and color composite with the same contours as the bottom. The bright blue source to the southwest of ADFS-27 is a star detected by *Gaia*. 870 μm beam sizes are indicated in the bottom left corners of two panels. 3 mm beam size is $2\farcs48 \times 1\farcs86$. Contours are in steps of $\pm 3\sigma$, where $1\sigma = 99$, 108, and 13.6 μJy beam^{-1} in the phase center for the robust 0.5 and natural weighting 870 μm and 3 mm data, respectively.

CO($J = 6 \rightarrow 5$)/CO($J = 5 \rightarrow 4$) line brightness temperature ratio of $r_{65} = 0.73 \pm 0.10$, which is consistent with the average value for SMGs within the uncertainties ($r_{65} = 0.66$; Bothwell et al. 2013), but significantly lower than that found in the $z = 5.3$ SMG AzTEC-3 ($r_{65} = 1.03 \pm 0.16$; Riechers et al. 2010). Thus, assuming the average CO($J = 5 \rightarrow 4$)/CO($J = 1 \rightarrow 0$) line brightness temperature ratio for SMGs of $r_{51} = 0.39$ (Carilli & Walter 2013), we find a CO($J = 1 \rightarrow 0$) luminosity of $L'_{\rm CO(1-0)} = 3.1 \times 10^{11}$ K km s^{-1} pc^2, i.e., $\sim$50$\times$ that of Arp 220 (e.g., Downes & Solomon 1998).[17] We also find a $H_2O(2_{11} \rightarrow 2_{02})$/CO($J = 6 \rightarrow 5$) ratio of $r_{\rm WC} = 0.25 \pm 0.14$, which is $\sim$2.5$\times$ lower than in Arp 220 and the $z = 6.34$ starburst HFLS3 (Rangwala et al. 2011; Riechers et al. 2013), and $\sim$1.5$\times$ lower than in the $z \sim 3.5$ strongly lensed starbursts G09v1.97 and NCv1.143 (Yang et al. 2016; D. A. Riechers et al. 2017, in preparation). This is consistent with a moderate interstellar medium excitation for a starburst system.

4. Analysis and Discussion

4.1. Spectral Energy Distribution Properties

To determine the overall SED properties of ADFS-27, we have fit modified blackbody (MBB) models to the continuum data between 1.25 μm and 3 mm (Figure 4).[18] We adopt the method described by Riechers et al. (2013) and Dowell et al. (2014), using an affine-invariant Markov Chain Monte Carlo (MCMC) approach, and joining the MBB to a ν^α power law on the blue side of the SED peak. We fit optically thin models, with the power-law slope α, the dust temperature $T_{\rm dust}$, and the spectral slope of the dust emissivity $\beta_{\rm IR}$ as fitting parameters, using the observed-frame 500 μm flux density as a normalization factor. We also fit "general" models that allow for wavelength-dependent changes in optical depth, adding the wavelength $\lambda_0 = c/\nu_0$, where the optical depth $\tau_\nu = (\nu/\nu_0)^{\beta_{\rm IR}}$ reaches unity as an additional fitting parameter.

The optically thin fitting procedure yields statistical mean values of $T_{\rm dust} = 59.9^{+42.7}_{-33.4}$ K, $\beta_{\rm IR} = 2.3^{+0.6}_{-1.1}$, and $\alpha = 6.2^{+5.0}_{-3.9}$.[19] The general fit yields mean values of $\lambda_0 = 195^{+39}_{-41}$ μm, $T_{\rm dust} = 55.3^{+7.8}_{-7.6}$ K, $\beta_{\rm IR} = 3.0^{+0.5}_{-0.5}$, and $\alpha = 9.8^{+6.7}_{-6.1}$. The fit also implies rest-frame infrared (8–1000 μm) and FIR (42.5–122.5 μm) luminosities of $L_{\rm IR} = 2.42^{+0.48}_{-0.47} \times 10^{13}\,L_\odot$ and $L_{\rm FIR} = 1.64^{+0.27}_{-0.27} \times 10^{13}\,L_\odot$, respectively.[20] Assuming a dust absorption coefficient of $\kappa_\nu = 2.64$ m^2 kg^{-1} at 125 μm (e.g., Dunne et al. 2003), we also find a dust mass of $M_{\rm dust} = 4.4^{+2.3}_{-2.4} \times 10^9\,M_\odot$.[21] Assuming a Chabrier (2003) stellar initial mass function, these parameters suggest a total SFR of $\sim$2400 $M_\odot$ yr^{-1}.

Given the limited SED constraints in the rest-frame optical, we obtain an estimate for the stellar mass $M_\star$ of ADFS-27 by normalizing the MAGPHYS-based SED template of HFLS3 in Figure 4 to the observed-frame 4.5 μm limit. This yields $M_\star < 1.2 \times 10^{11}\,M_\odot$.

4.2. Molecular Gas Mass, Gas-to-dust Ratio, and Gas Depletion Time

The $L'_{\rm CO(1-0)}$ value of ADFS-27 (based on the adopted $r_{51} = 0.39$) implies a total molecular gas mass of $M_{\rm gas} = 2.5 \times 10^{11}(\alpha_{\rm CO}/0.8)(0.39/r_{51})\ M_\odot$.[22] Taken at face value, this yields a gas-to-dust ratio of $M_{\rm gas}/M_{\rm dust} \simeq 60$, which is comparable to that in the $z = 6.34$ starburst HFLS3 and within the range of values found for nearby infrared-luminous galaxies (Wilson et al. 2008; Riechers et al. 2013), but

[17] Assuming the $r_{51} = 0.56$ value of AzTEC-3 instead would yield $L'_{\rm CO(1-0)} = 2.1 \times 10^{11}$ K km s^{-1} pc^2 (Riechers et al. 2010).

[18] Confusion noise and flux scale uncertainties were added in quadrature where appropriate.

[19] α is only poorly constrained by the data.

[20] The measured $L_{\rm IR}$ agrees to within $\sim$2% with independent estimates based on integrating a normalized MAGPHYS-based SED template based on the $z = 6.34$ starburst HFLS3 (Cooray et al. 2014), showing that the adopted power-law approximation of the short wavelength emission has a minor impact on the measured quantities.

[21] Given the limited photometry, the uncertainties may be somewhat underestimated.

[22] We here adopt a conversion factor of $\alpha_{\rm CO} = 0.8\,M_\odot$(K km s^{-1} pc^2)$^{-1}$ for nearby ultra-luminous infrared galaxies and SMGs (e.g., Downes & Solomon 1998; Tacconi et al. 2008).

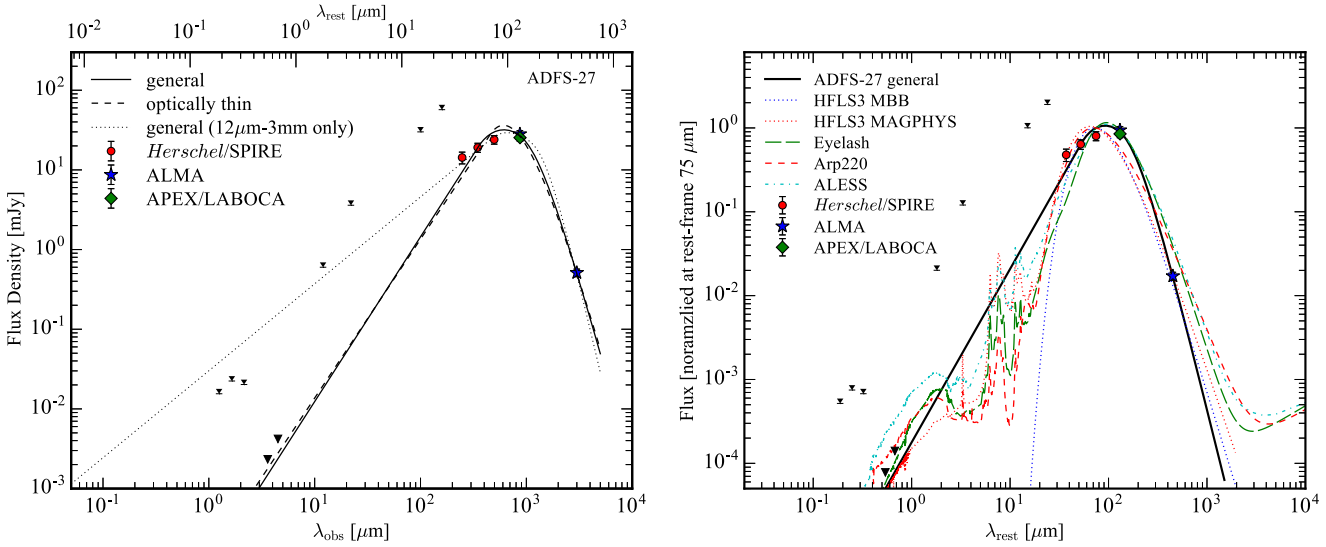

Figure 4. Spectral energy distribution of ADFS-27. The *Herschel*/SPIRE and APEX/LABOCA photometry were used for the initial selection of the source. Upper limits are from *Spitzer*/IRAC (deblended fluxes), *WISE,* and *Herschel*/PACS. Left: the solid line shows our best fit to the data. The dashed line shows the best fit assuming optically thin emission. The dotted line shows a fit to data at $\geqslant$12 μm only. Right: same, overplotted with template SEDs for the starbursts HFLS3 ($z = 6.34$; dotted lines), the Eyelash ($z = 2.33$; long dashed), and Arp 220 (dashed), and a composite for ALESS sources (dashed–dotted; Riechers et al. 2013; Cooray et al. 2014; Ivison et al. 2016) when normalized to the same rest-frame 75 μm flux density.

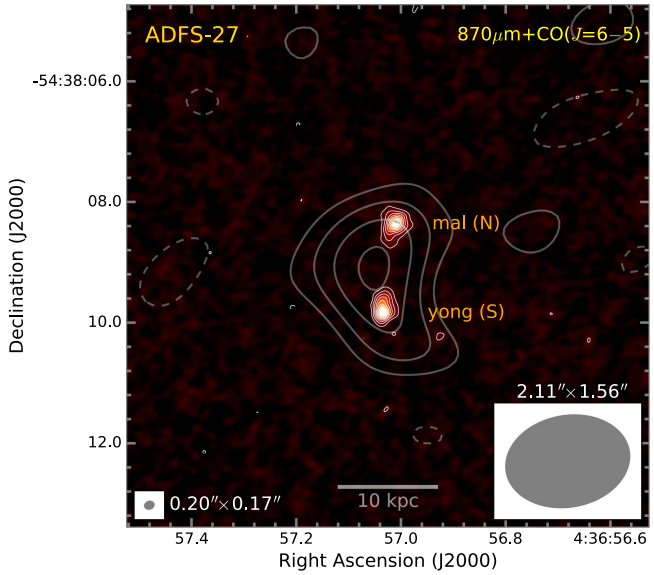

Figure 5. Overlay of ALMA CO($J = 6 \rightarrow 5$) emission (uniform weighting; gray contours) on 870 μm continuum emission (natural weighting; color scale and white contours) for ADFS-27. The CO velocity range is the same as in Figure 2. CO contours are shown in steps of $1\sigma = 0.23$ Jy km s^{-1} beam^{-1}, starting at $\pm 2\sigma$. CO beam size is indicated in the bottom right corner. 870 μm beam size (bottom left corner) and contour levels are the same as in Figure 3.

$\sim$4$\times$ lower than that for the $z = 5.30$ starburst AzTEC-3 (Riechers et al. 2014). At its current SFR, this implies a gas depletion time of $\tau_{\rm dep} = M_{\rm gas}/{\rm SFR} \simeq 100$ Myr, consistent with the general SMG population (e.g., Carilli & Walter 2013).

4.3. SFR and Gas Surface Densities, Gas Dynamics, and Conversion Factor

The apparent 870 μm continuum sizes of ADFS-27N (mal) and ADFS-27S (yong) imply physical sizes of $(1.83 \pm 0.18) \times (1.28 \pm 0.16)$ and $(2.05 \pm 0.18) \times (0.87 \pm 0.15)$ kpc^2 at $z = 5.655$, which are comparable to the $\sim$2.5 kpc diameters found for other $z > 4$ dusty starbursts like AzTEC-3, HFLS3, and SGP-38326 at similar wavelengths (Riechers et al. 2013, 2014; Oteo et al. 2016). Assuming that their flux ratios at 870 μm are representative at the peak of the SED, this implies $L_{\rm IR}$ surface densities of $\Sigma_{\rm IR} = 7.3$ and $7.5 \times 10^{12}\,L_\odot$ kpc^{-2} and SFR surface densities of $\Sigma_{\rm SFR} = 730$ and $750\,M_\odot$ yr^{-1} kpc^{-2}, at SFRs of $\sim$1350 and $1070\,M_\odot$ yr^{-1}, respectively, consistent with what is expected for "maximum starbursts" (e.g., Elmegreen 1999; Scoville 2003; Thompson et al. 2005). These $\Sigma_{\rm SFR}$ values are comparable to those found in other HyLIRGs at $z > 4$ like AzTEC-3, HFLS3, and SGP-38326 (Riechers et al. 2013, 2014; Oteo et al. 2016), but significantly higher than for the bulk of the DSFG population (e.g., Tacconi et al. 2006; Bussmann et al. 2013, 2015; Hodge et al. 2016).

Assuming a common CO linewidth and using the sizes and flux ratio measured in the 870 μm continuum emission, we can obtain approximate constraints on the dynamical masses $M_{\rm dyn}$ of ADFS-27N (mal) and ADFS-27S (yong) by adopting an isotropic virial estimator (e.g., Engel et al. 2010). We here increase the assumed source radii by a factor of 1.5 to account for the typical difference between the measured Gaussian sizes of gas and dust emission in SMGs, likely caused by decreasing dust optical depth toward the outskirts of the starbursting regions (e.g., Riechers et al. 2014). We find $M_{\rm dyn}^{\rm N} = 3.25 \times 10^{11}\,M_\odot$ and $M_{\rm dyn}^{\rm S} = 3.66 \times 10^{11}\,M_\odot$. Taken at face value, and conservatively assuming that 100% of

Table 2
Line Fluxes and Luminosities in ADFS-27

Transition	$I_{\rm line}$ (Jy km s^{-1})	$L'_{\rm line}$ (10^{10} K km s^{-1} pc^2)	$L_{\rm line}$ ($10^8\,L_\odot$)
CO($J = 5 \rightarrow 4$)	2.68 ± 0.20	11.96 ± 0.92	7.32 ± 0.56
CO($J = 6 \rightarrow 5$)	2.82 ± 0.34	8.73 ± 1.07	9.24 ± 1.13
$H_2O(2_{11} \rightarrow 2_{02})$[a]	0.83 ± 0.22	2.17 ± 0.58	2.96 ± 0.80

Note.
[a] Tentative detection. Independent confirmation is required. Quoted uncertainties are from Gaussian fitting to the line profile near the edge of the spectral range. We consider the true flux uncertainty to be at least $\sim$45%, consistent with line map-based estimates.

the dynamical mass is due to molecular gas (i.e., neglecting the potentially major contributions due to stellar mass and dark matter, and the likely minor contributions due to dust and black hole masses), this implies an upper limit of $\alpha_{\rm CO} < 2.25$ $M_\odot$(K km s^{-1} pc^2)$^{-1}$, which is consistent with the assumptions made above. This limit drops to $\alpha_{\rm CO} < 1.8\,M_\odot$(K km s^{-1} pc^2)$^{-1}$ when including the $M_\star$ limit at face value in the estimate. Adopting $\alpha_{\rm CO} = 0.8\,M_\odot$(K km s^{-1} pc^2)$^{-1}$ instead suggests gas fractions of $f_{\rm gas} = M_{\rm gas}/M_{\rm dyn} = 0.41$ and 0.32 for ADFS-27N and S, respectively. This is comparable to other SMGs (e.g., Carilli & Walter 2013; Riechers et al. 2013, 2014). Under the same assumptions, we find gas surface densities of $\Sigma^{\rm N}_{\rm gas} = 7.3$ and $\Sigma^{\rm S}_{\rm gas} = 8.1 \times 10^{10}\,M_\odot$ kpc^2. These values are at the high end of, but consistent with, the spatially resolved Schmidt–Kennicutt "star formation law" (e.g., Hodge et al. 2015), providing some of the first constraints on this relation at $z \sim 6$.

5. Conclusions

We have identified a massive, dust-obscured binary HyLIRG at a redshift of $z = 5.655$, using ALMA. Our target ADFS-27 was selected as an "870 μm riser," fulfilling an FIR color criterion of $S_{250\,\mu{\rm m}} < S_{350\,\mu{\rm m}} < S_{500\,\mu{\rm m}} < S_{870\,\mu{\rm m}}$. Among 25 *Herschel*-red sources (i.e., "500 μm risers," fulfilling $S_{250\,\mu{\rm m}} < S_{350\,\mu{\rm m}} < S_{500\,\mu{\rm m}}$) spectroscopically confirmed to date (e.g., Riechers et al. 2013; Riechers et al. 2017, in preparation) and ~300 photometrically identified *Herschel*-red sources (Asboth et al. 2016; Ivison et al. 2016; S. Duivenvoorden et al. 2017, in preparation), ADFS-27 is the only point source to fulfill this additional criterion, implying that such sources are likely very rare. Of the spectroscopic red sample, all sources are at $z < 5.5$ with the exception of HFLS3 at $z = 6.34$, which, however, had an additional criterion of $1.3 \times S_{350\,\mu{\rm m}} < S_{500\,\mu{\rm m}}$ applied in its selection (Riechers et al. 2013). ADFS-27 is significantly redder than HFLS3 in its 870 μm/500 μm color (1.06 versus 0.70). Of the 39 spectroscopically confirmed, 1.4 + 2.0 mm selected sample from the SPT survey, only SPT 0243–49 at $z = 5.6991$ fulfills the "870 μm riser" criterion (Strandet et al. 2016). While not providing a complete selection of $z \gg 5$ DSFGs, this shows the potentially very high median redshifts of such sources, which likely significantly exceeds that of the parent sample of red sources.[23] The apparent submillimeter fluxes of this source are ~3× higher than those of ADFS-27, but SPT 0243–49 is strongly gravitationally lensed and intrinsically less than half as bright as ADFS-27 (having two components of 6.2 and 5.2 mJy at 870 μm; Spilker et al. 2016). It thus is not a binary HyLIRG.

The overall properties of the binary HyLIRG ADFS-27 are perhaps most similar to lower-redshift sources like SGP-38326 at $z = 4.425$ (Oteo et al. 2016). It likely represents a major merger of two already massive galaxies ($>3 \times 10^{11}\,M_\odot$ each) at $z \sim 6$ leading to the formation of an even more massive galaxy, and it contains several billion solar masses of dust that must have formed at even earlier epochs. Its existence is consistent with previous findings of an apparently significantly higher space density of luminous dusty starbursts back to the first billion years of cosmic time than previously thought, which may be comparable to the space density of the most luminous quasars hosting supermassive black holes at the same epochs (e.g., Riechers et al. 2013; Asboth et al. 2016; Ivison et al. 2016). While the flux limits achieved by the deepest *Herschel* SPIRE surveys are perhaps not sufficiently sensitive to account for the bulk of dusty galaxies at $z > 5$, the population uncovered so far could be of key importance for understanding the early formation of some of the most massive quiescent galaxies at $z \gtrsim 3$ (e.g., Toft et al. 2014). Despite its extreme properties, ADFS-27 is only barely sufficiently bright and isolated to allow identification in the deep ADF-S SPIRE data. Of the >1000 deg^2 surveyed with SPIRE (e.g., Oliver et al. 2012), only ~110 deg^2 are sufficiently deep and high quality to identify "extremely red" sources as bright as ADFS-27 without the aid of strong gravitational lensing. Our results indicate that such sources are rare, with space densities as low as 9×10^{-3} deg^{-2} if our measurement is representative, but they could remain hidden in larger numbers among strongly lensed and/or 500 μm "dropout" samples with strong detections longward of 850 μm, identified in large-area surveys with JCMT/SCUBA-2, APEX/LABOCA, ACT, and SPT, and future facilities like CCAT-prime.

The authors thank the anonymous referee for a helpful and constructive report. The National Radio Astronomy Observatory is a facility of the National Science Foundation operated under cooperative agreement by Associated Universities, Inc. This paper makes use of the following ALMA data: ADS/JAO.ALMA# 2016.1.00613.S and ADS/JAO.ALMA# 2013.1.00001.S. ALMA is a partnership of ESO (representing its member states), NSF (USA) and NINS (Japan), together with NRC (Canada) and NSC and ASIAA (Taiwan), in cooperation with the Republic of Chile. The Joint ALMA Observatory is operated by ESO, AUI/NRAO and NAOJ. D.R. acknowledges support from the National Science Foundation under grant number AST-1614213 to Cornell University. T.K.D.L. acknowledges support by the NSF through award SOSPA4-009 from the NRAO. I.P.F., R.M.C., and P.M.N. acknowledge support from the Spanish Ministerio de Economia y Competitividad (MINECO) under grant number ESP2015-65597-C4-4-R. This research makes use of data obtained with *Herschel,* an ESA space observatory with science instruments provided by European-led Principal Investigator consortia and with important participation from NASA, through the HerMES project. HerMES is a *Herschel* Key Program utilizing Guaranteed Time from the SPIRE instrument team, ESAC scientists and a mission scientist. This work is based in part on observations made with the *Spitzer Space Telescope*, which is operated by the Jet Propulsion Laboratory, California Institute of Technology under a contract with NASA. This publication made use of data products from the *Wide-field Infrared Survey Explorer,* which is a joint project of the University of California, Los Angeles, and the Jet Propulsion Laboratory/California Institute of Technology, funded by the National Aeronautics and Space Administration. This work is based on observations made with APEX under Program ID: M-090.F-0025-2012, and also based on observations obtained as part of the VISTA Hemisphere Survey, ESO Progam 179.A-2010 (PI: McMahon).

Facilities: ALMA, APEX(LABOCA), *Herschel*(PACS and SPIRE), *Spitzer*(IRAC), *WISE*, ESO:VISTA.

[23] SPT 0459–59 at $z = 4.7993$ does not fulfill the selection criterion with the revised LABOCA 870 μm flux of (61 ± 8) mJy found by Spilker et al. (2016). However, our discussion would remain largely unchanged if we included this source.

ORCID iDs

Dominik A. Riechers https://orcid.org/0000-0001-9585-1462
Rob J. Ivison https://orcid.org/0000-0001-5118-1313
Rui Marques-Chaves https://orcid.org/0000-0001-8442-1846
Iván Oteo https://orcid.org/0000-0001-5875-3388
Dave L. Clements https://orcid.org/0000-0002-9548-5033
Seb Oliver https://orcid.org/0000-0001-7862-1032
Douglas Scott https://orcid.org/0000-0002-6878-9840
Axel Weiss https://orcid.org/0000-0003-4678-3939

References

Asboth, V., Conley, A., Sayers, J., et al. 2016, MNRAS, 462, 1989
Blain, A. W., Smail, I., Ivison, R. J., Kneib, J.-P., & Frayer, D. T. 2002, PhR, 369, 111
Bothwell, M. S., Smail, I., Chapman, S. C., et al. 2013, MNRAS, 429, 3047
Bussmann, R. S., Pérez-Fournon, I., Amber, S., et al. 2013, ApJ, 779, 25
Bussmann, R. S., Riechers, D., Fialkov, A., et al. 2015, ApJ, 812, 43
Capak, P., Carilli, C. L., Lee, N., et al. 2008, ApJL, 681, L53
Capak, P. L., Riechers, D., Scoville, N. Z., et al. 2011, Natur, 470, 233
Carilli, C. L., & Walter, F. 2013, ARA&A, 51, 105
Casey, C. M., Narayanan, D., & Cooray, A. 2014, PhR, 541, 45
Chabrier, G. 2003, PASP, 115, 763
Chapman, S. C., Blain, A. W., Smail, I., & Ivison, R. J. 2005, ApJ, 622, 772
Combes, F., Rex, M., Rawle, T. D., et al. 2012, A&A, 538, L4
Cooray, A., Calanog, J., Wardlow, J. L., et al. 2014, ApJ, 790, 40
Cox, P., Krips, M., Neri, R., et al. 2011, ApJ, 740, 63
Daddi, E., Dannerbauer, H., Stern, D., et al. 2009, ApJ, 694, 1517
Davé, R., Finlator, K., Oppenheimer, B. D., et al. 2010, MNRAS, 404, 1355
Dowell, C. D., Conley, A., Glenn, J., et al. 2014, ApJ, 780, 75
Downes, D., & Solomon, P. M. 1998, ApJ, 507, 615
Dunne, L., Eales, S. A., & Edmunds, M. G. 2003, MNRAS, 341, 589
Elmegreen, B. G. 1999, ApJ, 517, 103
Engel, H., Tacconi, L. J., Davies, R. I., et al. 2010, ApJ, 724, 233
Fu, H., Cooray, A., Feruglio, C., et al. 2013, Natur, 498, 338
Fudamoto, Y., Ivison, R. J., Oteo, I., et al. 2017, MNRAS, 472, 2028
Hayward, C. C., Jonsson, P., Kereš, D., et al. 2012, MNRAS, 424, 951
Hodge, J. A., Riechers, D., Decarli, R., et al. 2015, ApJL, 798, L18
Hodge, J. A., Swinbank, A. M., Simpson, J. M., et al. 2016, ApJ, 833, 103
Ivison, R. J., Lewis, A. J. R., Weiss, A., et al. 2016, ApJ, 832, 78
Ivison, R. J., Papadopoulos, P. P., Smail, I., et al. 2011, MNRAS, 412, 1913
Ivison, R. J., Smail, I., Barger, A. J., et al. 2000, MNRAS, 315, 209
Ivison, R. J., Smail, I., Le Borgne, J.-F., et al. 1998, MNRAS, 298, 583
Ivison, R. J., Swinbank, A. M., Smail, I., et al. 2013, ApJ, 772, 137
Narayanan, D., Hayward, C. C., Cox, T. J., et al. 2010, MNRAS, 401, 1613
Narayanan, D., Turk, M., Feldmann, R., et al. 2015, Natur, 525, 496
Nguyen, H. T., Schulz, B., Levenson, L., et al. 2010, A&A, 518, L5
Oliver, S. J., Bock, J., Altieri, B., et al. 2012, MNRAS, 424, 1614
Oteo, I., Ivison, R. J., Dunne, L., et al. 2016, ApJ, 827, 34
Rangwala, N., Maloney, P. R., Glenn, J., et al. 2011, ApJ, 743, 94
Riechers, D. A., Bradford, C. M., Clements, D. L., et al. 2013, Natur, 496, 329
Riechers, D. A., Capak, P. L., Carilli, C. L., et al. 2010, ApJL, 720, L131
Riechers, D. A., Carilli, C. L., Capak, P. L., et al. 2014, ApJ, 796, 84
Riechers, D. A., Hodge, J., Walter, F., Carilli, C. L., & Bertoldi, F. 2011, ApJL, 739, L31
Schulz, B., Marton, G., Valtchanov, I., et al. 2017, arXiv:1706.00448
Scoville, N. 2003, JKAS, 36, 167
Spilker, J. S., Marrone, D. P., Aravena, M., et al. 2016, ApJ, 826, 112
Strandet, M. L., Weiss, A., Vieira, J. D., et al. 2016, ApJ, 822, 80
Tacconi, L. J., Genzel, R., Smail, I., et al. 2008, ApJ, 680, 246
Tacconi, L. J., Neri, R., Chapman, S. C., et al. 2006, ApJ, 640, 228
Thompson, T. A., Quataert, E., & Murray, N. 2005, ApJ, 630, 167
Toft, S., Smolčić, V., Magnelli, B., et al. 2014, ApJ, 782, 68
Walter, F., Decarli, R., Carilli, C., et al. 2012, Natur, 486, 233
Weiss, A., De Breuck, C., Marrone, D. P., et al. 2013, ApJ, 767, 88
Wilson, C. D., Petitpas, G. R., Iono, D., et al. 2008, ApJS, 178, 189
Yang, C., Omont, A., Beelen, A., et al. 2016, A&A, 595, A80